galaxies

MDPI

Article

Resonant Effects of a Bar on the Galactic Disk Kinematics Perpendicular to Its Plane

Vladimir Korchagin [1,*], Artem Lutsenko [2], Roman Tkachenko [1], Giovanni Carraro [2] and Katherine Vieira [3]

[1] Institute of Physics, Southern Federal University, Stachki Avenue 124, 344090 Rostov-on-Don, Russia; rtkachenko@sfedu.ru
[2] Dipartimento di Fisica e Astronomia, Università di Padova, Vicolo Osservatorio 3, I-35122 Padova, Italy; artem.lutsenko@studenti.unipd.it (A.L.); giovanni.carraro@unipd.it (G.C.)
[3] Instituto de Astronomía y Ciencias Planetarias, Universidad de Atacama, Copayapu 485, Copiapó 1531772, Chile; katherine.vieira@uda.cl
* Correspondence: vkorchagin@sfedu.ru

Abstract: Detailed analysis of kinematics of the Milky Way disk in the solar neighborhood based on the GAIA DR3 catalog reveals the existence of peculiarities in the stellar velocity distribution perpendicular to the galactic plane. We study the influence of resonances—the outer Lindblad resonance and the outer vertical Lindblad resonance—of a rotating bar with stellar oscillations perpendicular to the plane of the disk, and their role in shaping the spatial and the velocity distributions of stars. We find that the Z and V_Z distributions of stars with respect to L_Z are affected by the outer Lindblad resonance. The existence of bar resonance with stellar oscillations perpendicular to the plane of the disk is demonstrated for a long (large semi-axis 5 kpc) and fast rotating bar with $\Omega_b = 60.0$ km s^{-1} kpc^{-1}. We show also that, in the model with the long and fast rotating bar, some stars in the 2:1 OLR region deviate far from their original places, entering the bar region. A combination of resonance excitation of stellar motions at the 2:1 OLR region together with strong interaction of the stars with the bar potential leads to the formation of the group of 'escapees', i.e., stars that deviate in R and Z—directions at large distances from the resonance region. Simulations, however, do not demonstrate any noticeable effect on V_Z-distribution of stars in the solar neighborhood.

Keywords: Milky Way disk; kinematics; dynamics

Citation: Korchagin, V.; Lutsenko, A.; Tkachenko, R.; Carraro G.; Vieira, K. Resonant Effects of a Bar on the Galactic Disk Kinematics Perpendicular to Its Plane. *Galaxies* **2023**, *11*, 97. https://doi.org/10.3390/galaxies11050097

Academic Editor: Yosuke Mizuno

Received: 31 May 2023
Revised: 1 September 2023
Accepted: 4 September 2023
Published: 6 September 2023

1. Introduction

Since the HIPPARCOS era it has been known that the solar neighborhood manifests complex dynamical structures such as streams and moving groups. The Gaia mission [1–4], with its accurate observational data, shed new light the on properties of kinematical and structural peculiarities, both in the solar neighborhood and beyond. Examples of such structures are the *ridges* (diagonal distributions in the (R, V_ϕ) plane) and *arches*, phase spirals in the (Z, V_Z) plane, bimodality in (V_R, V_ϕ) plane including the Hercules stream [5,6], and vertical waves [7].

Many of the abovementioned kinematical and structural features are related to the resonant phenomena occurring within the Galactic disk. Resonances cause the radial migration of the stars that in turn affect the disk's density distribution and its kinematical properties. Schönrich and Binney [8] distinguished two types of radial migration caused by resonance phenomena. In the first type, the angular momentum of a star changes, so the star's orbit moves inwards or outwards, depending on whether the angular momentum is lost or gained. This type of resonance occurring in stellar disks was studied by Sellwood and Binney [9] and Roškar et al. [10], who showed that the resonant interaction of stars with a spiral density wave churns the stars around corotation causing their re-distribution within the Galactic disk. As was stressed by Sellwood and Binney [9],

such behavior has profound consequences for the chemical evolution of galaxies. Similar 'churning' of matter within corotation resonance in gaseous gravitating disks was shown by Laughlin and Korchagin [11] who found that an unstable spiral density wave depletes mass around the corotation, leading eventually to an amplitude saturation of an unstable spiral. If a star-periodic gravitational field interaction increases a star's epicycle amplitude without changing its angular momentum, the star contributes to the density over a wider range of radii. Schönrich and Binney [8], in modification of the terminology introduced by Sellwood and Binney [9], called theses changes in the epicycle amplitude 'blurring'.

Dehnen [12] demonstrated that a fast rotating bar with corotation resonance located at 3.5–5 kpc causes a bimodal distribution of stars in the (V_R, V_ϕ) plane at the outer Lindblad resonance (OLR). This idea was further confirmed by Antoja et al. [13] and Monari et al. [14] who explained the bimodality in (V_R, V_ϕ) as a result of the bar interaction with the stars at the 2:1 OLR.

Hunt and Bovy [15] discussed another possibility to account for the observed kinematical peculiarity in the solar neighborhood—the Hercules stream, by the 4:1 OLR resonance with a slowly rotating bar. Hunt et al. [16] demonstrated that the Hercules stream and the observed ridges in the (R, V_ϕ) plane can be explained by transient winding spiral arms, independently or in combination with a long and slow bar. It is also known that ridges can be produced by a barred potential and its resonances [5].

Antoja et al. [5] demonstrated recently the existence of a phase-spiral pattern seen in the solar neighborhood in the (Z, V_Z)—plane. The plausible explanation of the appearance of the Gaia phase-space spiral is a passage through the Milky Way disk of the Sagittarius dwarf galaxy about 400 ± 150 Myr ago (see Antoja et al. [5], Binney and Schönrich [17] and Tepper-García et al. [18]). Alternatively, the observed feature can be explained by disk perturbations from the subhalos [19], a perturbation generated by a buckling bar [20], and a misaligned gas accretion [21]. In addition to the influence of resonances on dynamic structures and phase-space mixing [5,16,22], the influence of the resonance effects on chemical evolution of the Galactic disk is also well known [23–26].

Resonances of an external perturbing potential with the stellar motions in the direction perpendicular to the Galactic plane were first considered by Binney [27]. These resonances, however, were not studied in much detail. Combes et al. [28] demonstrated that vILR-inner resonance of the bar with the vertical motions of the stars can be responsible for the formation of the bar's peanut shape. Further, the influence of vertical inner Lindblad resonances on the formation of X- or peanut-shaped Galactic bulges was discussed by Quillen [29] and Quillen et al. [30]. The resonant thickening of self-gravitating disks was analytically studied by Fouvry et al. [31]. Recently, Vieira et al. [32] presented a detailed analysis of kinematics of the Milky Way disk in the solar neighborhood using the GAIA DR3 catalogue. The authors found an excess of stars in the V_Z-distribution of red giants in the solar neighborhood at $-40 < V_Z < -20$ km s^{-1} and a dearth of stars in the V_Z distribution at $25 < V_Z < 50$ km s^{-1}.

The discovery of dips and bumps in the V_Z-velocity distribution of stars in the solar neighborhood (Vieira et al. [32]) posed the question if the development of such features can be caused by the resonance of the rotating bar with the stellar motions perpendicular to the galactic disk in the solar neighborhood. The resonances of a rotating bar with stellar motions in the plane of the disk lead to a considerable reshuffling of matter within the plane of the disk and can also influence the kinematical and density distributions of stars in a Galactic disk in the direction perpendicular to the disk's plane.

We study in this paper how the resonances of the stellar motions with a rotating bar, occurring in the solar neighborhood, namely, 2:1 outer Lindblad resonance, 1:1 outer Lindblad resonance, and the vertical outer Lindblad resonance can influence the disk's kinematical properties, in particular, the peculiar kinematical features reported by Vieira et al. [32].

Section 2 describes the method we chose to study the resonance dynamics of the thin disk stars under non-axisymmetric time-dependent bar potentials. Section 3 presents the results of our study. Section 4 gives a brief summary of our results.

2. The Model

We study the influence of the bar on the dynamics of a thin collisionless disk, aiming at possible detection of resonance effects, both in the plane of the disk and perpendicular to disk's plane. The behaviour of a thin collisionless disk is simulated with help of the astrophysical package `Galpy` [33], by integrating the particle dynamics using Dormand–Prince method (`dop853`) [34]—the eighth order Runge–Kutta family method with the adaptive timesteps. To generate the equilibrium collisionless disk, we followed the dynamics of the initial velocity and density distribution of particles in the Milky Way-like potential during three Gyr until the equilibrium distribution of stars is achieved. We then study the dynamics of the resulting equilibrium configuration for another three Gyr, while considering the influence of the bar potential. We assume that the bar smoothly switches on over a period of one Gyr after the axisymmetric equilibrium of the disk is settled. We find that the integration time of three Gyr is sufficient to study the influence of the bar—further increase of integration time does not lead to the qualitative change of disk dynamics.

2.1. Initial Distribution

As it was mentioned above, we discuss the dynamics of a thin Galactic disk, taking into account the possible influence of a bar. We are interested in the influence of resonances with a bar outside the bar region; therefore, the stellar spatial distribution was generated outside four kpc using 10^6 particles and assuming the commonly accepted exponential density distribution law $\propto \exp\{-r/r_d\}$, where r_d is the radial scale length of the Galactic thin disk. There is a fairly large spread of the measured values of r_d ranging from two to four kpc [35–38]. Following Jurić et al. [39], we choose in this paper the value of $r_d = 2.5$ kpc. For the vertical distribution of particles, we use the exponential law $\propto \exp\{-z/h_z\}$ with the adopted value for vertical scale height of $h_z = 300$ pc [39,40]. Average velocities of the particles in the radial direction and in the direction perpendicular to the disk were chosen to be zero $< V_R > = 0$ and $< V_Z > = 0$ km s^{-1}. To generate mean velocities of the particles in the azimuthal direction $< V_\phi >$, we use the disk's rotation curve in the axisymmetric Galactic potential `McMillan17` [41] (from now on MC17), described in detail in next subsection. We adopt the values of the velocity dispersions of particles in the solar neighborhood $\sigma_R, \sigma_\phi, \sigma_Z$ equal to 31, 20 and 11 km s^{-1} Vieira et al. [32]. The dependence of the velocity dispersion of particles on the radius was adopted in the form $\sigma_R = \sigma_{R,0}/\exp(r/7.4\,[\mathrm{kpc}])$, taken from Khrapov et al. [38], Tiede and Terndrup [42] where $\sigma_{R,0} = 93$ km s^{-1} to satisfy the observed value of the velocity dispersion in the solar neighborhood of $\sigma_R = 31$ km s^{-1}. The azimuthal velocity dispersion was set using the equilibrium condition for the collisionless disk [38]:

$$\sigma_\varphi = \sigma_R \frac{\varkappa}{2\Omega}, \tag{1}$$

where Ω and $\varkappa$ are the angular velocity and the epicyclic frequency of the disk calculated from the equilibrium rotation curve in the MC17 potential. For setting the velocity dispersion perpendicular to the disk direction, we use the ration $\sigma_Z/\sigma_R = 0.36$ to satisfy the observed value of σ_Z velocity dispersion in the solar neighborhood $\sigma_Z = 11$ km s^{-1}.

2.2. Galactic Potential Models

We adopt the axisymmetric model of the Galactic potential from [41], which includes potentials of the bulge, the thin and the thick disks, the gravitational potentials of the gaseous (H_1 and H_2) disks, and the gravitational potential of the dark matter halo.

To model the time-dependent potential of a rotating bar, we add to the MC17 potential model a potential of a smoothly growing for one Gyr bar, using the prescription taken from Dehnen [12]:

$$A(t) = \left(\frac{3}{16}\xi^5 - \frac{5}{8}\xi^3 + \frac{15}{16}\xi + \frac{1}{2}\right), \quad (2)$$

where $\xi = 2(\frac{t-t_{form}}{t_{steady}}) - 1$, when $t_{form} \leq t \leq t_{form} + t_{steady}$; $\xi = -1$, when $t \leq t_{form}$ and $\xi = 1$, when $t \geq t_{form} + t_{steady}$. The amplitude multiplier function $A(t)$ smoothly changes from 0 to 1 for one Gyr, so the bar potential is smoothly turned on after the equilibrium axisymmetric distribution is settled.

The bar potential is modeled by the equation taken from Long and Murali [43]:

$$\Phi_r(x, y, z) = \frac{GM_b}{2a} \ln\left(\frac{x - a + T_-}{x + a + T_+}\right). \quad (3)$$

Here, $T_\pm = [(a \pm x)^2 + y^2 + (b + \sqrt{c^2 + z^2})^2)]^{1/2}$. a, b, c are characteristic bar parameters and x, y, z are Cartesian coordinates. We adopt values of bar semi-axes equal to $b = 1$ kpc, $c = 0.3$ kpc. For the major semi-axis of the bar, a, we adopt two values: $a = 5$ kpc—the long bar, (LB) and $a = 3.5$ kpc—the short bar (SB). In accordance with Portail et al. [44] and Kent [45], we choose the bar mass equal to $M_b = 1.88 \times 10^{10}$ $M_\odot$, which is also in a agreement with the estimate of Zhao et al. [46].

A number of studies have been undertaken to measure the bar angular velocity [47–51]. Debattista et al. [47] estimated the angular velocity of the Galactic bar to be $\Omega_b = 59 \pm 5$ km s^{-1} kpc^{-1}. Recent data based on Gaia proper motion measurements allowed for a more accurate estimation of the pattern speed of the Galactic bar. However, there is still disagreement between the results. For example, Sanders et al. [48] used the VVV Infrared Astrometric Catalogue (VIRAC) and Gaia DR2 proper motions and estimated the angular velocity of the bar to be $\Omega_b = 41 \pm 3$ km s^{-1} kpc^{-1}, Clarke et al. [49] obtained the value of $\Omega_b = 37.5$ km s^{-1} kpc^{-1} [50]. Dehnen [12] suggested that, to explain some kinematical features observed in the solar neighborhood, a bar with the angular velocity of $\Omega_b = 55.5$ km s^{-1} kpc^{-1} is required. The fast bar is also supported by some other studies [13,52–54] with the bar angular velocity varying within $\Omega_b = 55$–60 km s^{-1} kpc^{-1}. We use in this paper two values of the angular velocity of the bar: $\Omega_b = 40$ km s^{-1} kpc^{-1} (slow bar) and 60 km s^{-1} kpc^{-1} (fast bar). Thus, we explore two values of the angular velocity of a bar and the two values of the bar's major semi-axis. We use the following designations for our models. The model with the fast long bar ($\Omega_b = 60$ km s^{-1} kpc^{-1}, $a = 5$ kpc) is designated as "LB60", and the slow short bar ($\Omega_b = 40$ km s^{-1} kpc^{-1}, $a = 3.5$ kpc) is designated as "SB40". The models we use are listed in Table 1.

Table 1. List of different bar models.

Name	Ω_b [km s^{-1} kpc^{-1}]	a [kpc]
SB40	40	3.0
SB60	60	3.0
LB40	40	5.0
LB60	60	5.0

Here Ω_b is angular bar velocity and a is the bar major semi-axis.

2.3. Rotation Curves

The rotation curves of our barred, and non-barred models are shown in Figure 1. In the bar potential, the rotational curve is systematically higher compared to that in the axisymmetric model MC17 due to the fact that a bar with mass $M_b = 1.88 \times 10^{10}$ $M_\odot$ is added to the axisymmetric MC17 model. The rotation curves were determined from the equation $v_{rot} = (rd\Phi/dr)^{1/2}$, where Φ represents the total potential in the plane Z = 0. With the bar potential the disk rotation is not circular in its central regions, so the "rotation curve" depends now on the direction relative to the bar major axis. Figure 1 presents the rotation curves calculated along a few directions relative to the bar major axis. As one can

see from Figure 1, with the adopted mass of the bar of 1.88×10^{10} $M_{\odot}$, which is comparable to that of the unperturbed axisymmetric disk, the bar changes the disk's rotation, which shifts the position of corotation resonance from ≈ 3.8 kiloparsecs in the MC17 model to about 5 kps. The long bar model satisfies the criterion of Contopoulos [55], for which $\mathbb{R} = R_{CR}/R_{bar} \geq 1$. We also notice that the position of corotation is important for studying the particle dynamics at corotation resonance, but is not of much importance in our study focused on disk dynamics at the outer and the vertical outer Lindblad resonances.

The galactocentric distance of the Sun is chosen to be $R_{\odot} = 8.122$ kpc (GRAVITY Collaboration et al. [56]).

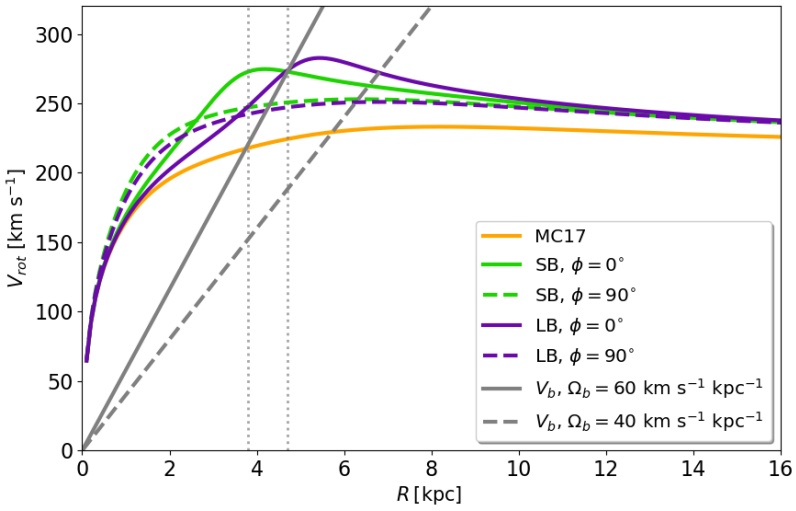

Figure 1. Rotation curves of axisymmetric (orange line) and non-axisymmetric models. For the models with bars, the rotation curves are shown for different directions with respect to the bar major semi-axis. Short bar—green lines. Long bar—purple lines. Grey lines—the linear rotation curves corresponding to the angular velocities of a bar. The vertical lines mark the positions of corotation in MC17 model and in the models with the bar.

2.4. Resonances

2.4.1. Resonances in the Plane of the Disk

Resonances in the Galactic plane of the disk are determined by the condition:

$$m(\Omega_b - \Omega) = l\kappa\,, \tag{4}$$

where κ is the epicyclic frequency, l and m are integer numbers equal to $(l = 0, \pm 1, \pm 2, ...)$ and $(m = 1, 2, ...)$. We use the following notation for resonances: if $(m, l) = (2, -1)$, $(2, 1)$, $(1, 1)$, this determines the 2:1 inner Lindblad resonance (2:1 ILR) and 2:1 outer Lindblad resonance (2:1 OLR) and 1:1 outer Lindblad resonance (1:1 OLR). We consider the dominating $m = 2$ and $m = 1$ modes in the bar potential, neglecting higher order modes. It should be noticed, however, that $m = 4$ Fourier component of the bar potential can influence the disk dynamics as shown by Hunt and Bovy [15]. The corotation resonance (CR) is determined by the conditions $l = 0$, when the rotation frequency of the stars is equal to the bar pattern frequency.

Figure 2 shows the positions of ILR, OLR and CR resonances in the plane of the disk in our models for bar pattern speeds $\Omega_b = 40\,\mathrm{km\,s^{-1}\,kpc^{-1}}$ and 60 $\mathrm{km\,s^{-1}\,kpc^{-1}}$.

Our focus is on the study of the resonance effects in the solar neighborhood and beyond, so we exclude from consideration the disk dynamics in the central regions of the disk—namely, the inner Linblad resonance and corotation.

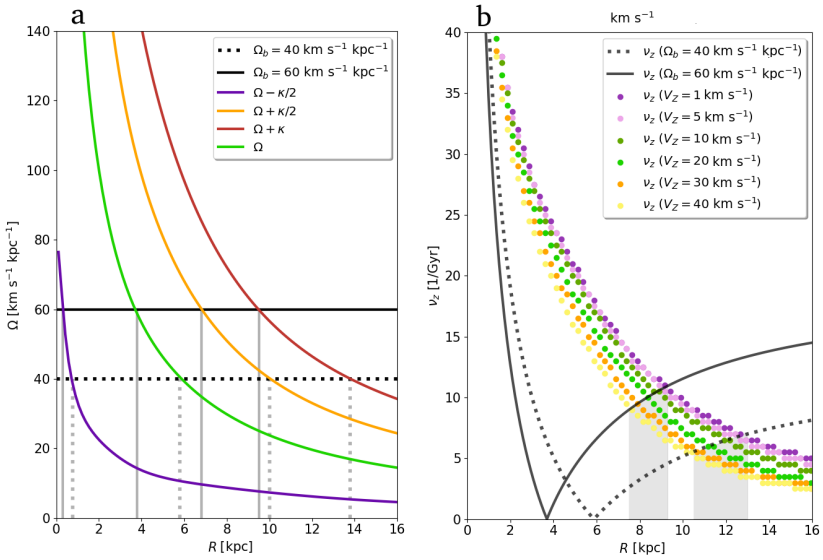

Figure 2. The positions of resonances in the plane of the disk (**a**) and in perpendicular to the disk direction (**b**). (**a**) Black solid and dotted horizontal lines are the angular velocities of the bar. Purple, green and orange lines show the radial dependence of the quantities $\Omega - \kappa/2$, Ω, $\Omega + \kappa/2$ and $\Omega + \kappa$, respectively. The vertical lines mark the positions of 2:1 ILR, CR, 2:1 OLR and 1:1 OLR resonances. (**b**) Frequencies of oscillations of particles (colored dots) perpendicular to the disk as a function of galactocentric radius. Black solid and dotted lines show the radial dependence of frequency of vertical oscillations, ν_Z in the left hand side of the Equation (5). Crossings correspond to the positions of the 2:1 vertical outer Lindblad resonance (2:1 vOLR) in the disk.

2.4.2. Vertical Resonances

Resonance between oscillation of a star in the direction perpendicular to the plane of the disk and rotating perturbing potential that has m-fold rotational symmetry occurs when the following condition is met [27,57,58]:

$$m(\Omega_b - \Omega) = l\Omega_Z\,, \tag{5}$$

where l is an integer number.

We will be interested in resonance condition when $l = +1$ because, for larger values of l, resonance conditions are achieved far from the solar neighborhood. The value of m we assume to be equal to $m = 2$. We study thus an influence of the vertical outer 2:1 Lindblad resonance (2:1 vOLR). Ω_Z is the frequency of the vertical oscillations, which we will use further in the form of $\nu_Z = \Omega_Z/2\pi$, where ν_Z is the linear frequency of oscillations.

In the direction perpendicular to the disk, its density and potential are changing rapidly so the periods of oscillations of the particles depend on their velocities in the Z-direction at $Z = 0$ and have to be determined separately. To find the positions of the vertical resonance, we measure the frequencies of the vertical oscillations of particles by direct integration of the orbits of particles in the axisymmetric potential. To do this, we generate at different radii of the disk the particles that have velocities perpendicular to the disk's plane equal to $V_Z = 1, 5, 10, 20, 30, 40$ km s^{-1}, and the azimuthal velocities corresponding to the equilibrium rotational velocity at a given radius. We also assume that $V_R = 0$ km s^{-1}. To estimate the frequencies, we followed the dynamics of the particles during a fixed period of time and calculated the number of intersections of the particles with the mid-plane of the disk. Results of simulations, covering the range of V_Z-velocities in the solar neighborhood, are shown in Figure 2b. We notice that frequencies of particle oscillations are in agreement with the results of Antoja et al. [5]. Beraldo e Silva et al. [59] used the python package `naif` for the frequency analysis of orbits. In this paper, we determined the frequencies of the non-linear oscillations from the numerical simulations that we deem sufficient for our purpose.

Figure 2b shows the positions of the vertical resonances in our mock Galactic disk, determined in this way. Black solid and dotted lines demonstrate the radial dependence of the theoretical frequency ν_Z from Equation (5) as a function of radius for two values of the bar angular velocity $\Omega_b = 40\,\mathrm{km\ s^{-1}\ kpc^{-1}}$ and 60 $\mathrm{km\ s^{-1}\ kpc^{-1}}$. The positions of the vertical resonances are marked in Figure 2b by the grey zones.

As one can see from Figure 2b, the resonance of stellar motions with a bar that has an angular velocity of $\Omega_b = 40\,\mathrm{km\ s^{-1}\ kpc^{-1}}$ occurs at ≈11–13 kpc, while resonance with the fast rotating bar that has $\Omega_b = 60\,\mathrm{km\ s^{-1}\ kpc^{-1}}$ occurs at ≈8–9 kpc.

When analyzing the resonance regions, it is important to know variations of the vertical force K_Z in the models with the Galactic bar $K_Z = -\partial\Phi/\partial Z$. Figure 3 shows the radial dependence of the Z-component of the gravitational force taken at Z = 200 pc and Z = 500 pc for the axisymmetric MC17 potential and for two models with bar major semi-axis a = 3.5 (SB) and a = 5 (LB) kpc. With the bar potential, the calculations are carried out in three different directions with respect to the large semi-axis: 0°, 45° and 90°. The amplification of oscillations of the particles perpendicular to the plane of the disk is caused by the periodic force from the non-axisymmetric rotating bar potential. The efficiency of such amplification of particle oscillations is determined by the difference of the bar gravitational force acting perpendicular to the disk in the direction of the bar's major and minor axes.

As one can see from the Figure 3, for the long bar (LB) model the variation of the force at the R = 9 kpc is about 10%, while at R = 13 kpc the force variation is about 4%. For the short bar (SB), variation of gravitational force caused by the bar is about 3% at the R = 9 kpc, and at R = 13 kpc.

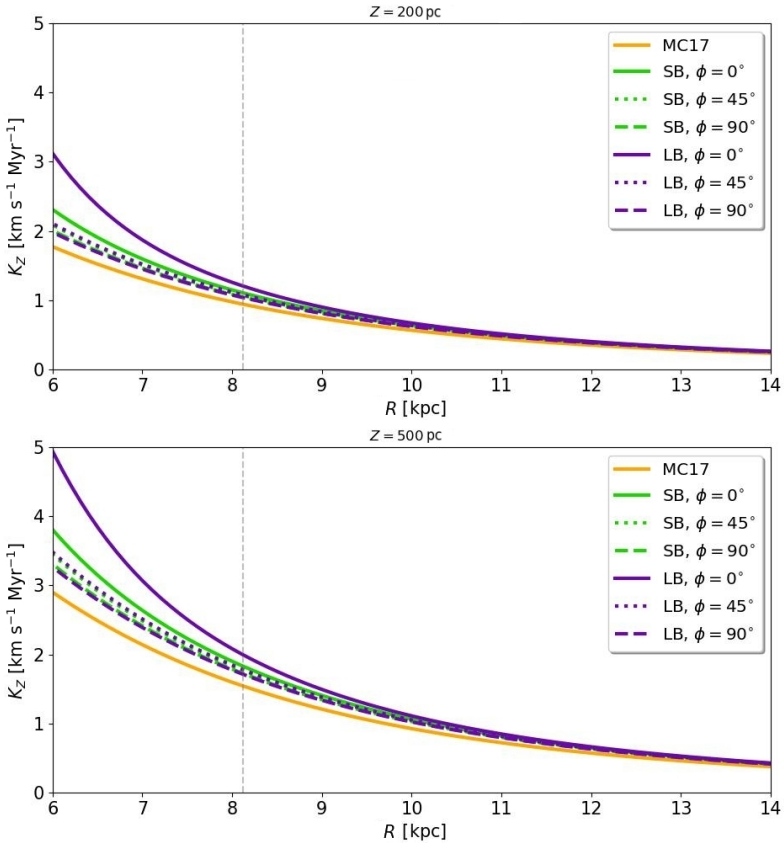

Figure 3. Radial dependence of the vertical component of the force for the axisymmetric MC17 potential (orange) and potentials with the bar with major semi-axis a = 3.5 kpc (green) and a = 5 kpc (purple). For models with the bar, the force dependence is shown for different angles with respect to the bar major axis. The vertical gray line marks the position of the Sun.

3. Results and Discussion

3.1. Equilibrium in the Axisymmetric Potential

To construct the axisymmetric equilibrium distribution in the MC17 potential model, we integrate the dynamics of the initially generated distribution of particles for five Gyr. Figure 4 shows the result of such integration. After ≈ three Gyr of integration the disk rebuilds itself and reaches equilibrium, remaining unchanged during further integration, with the radial scale length of the disk beyond four kpc approximately equal to its initial value of $r_d = 2.5$ kpc.

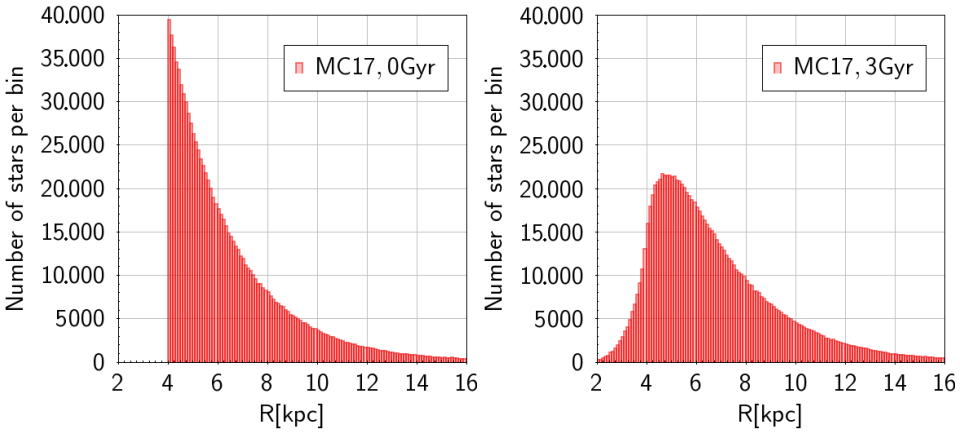

Figure 4. Evolution of the particle distribution in the MC17 model from the initial distribution (**left**) to the equilibrium one after three Gyr of evolution. The size of the radial bins is 0.1 kpc.

Figure 5 shows the distributions along the radius of the particles Z-coordinate (first column), velocity component perpendicular to the disk V_Z (second column), azimuthal velocity V_ϕ (third column), and the radial velocity of the particles V_R (fourth column) of the initially generated distribution of particles (first row) and the equilibrium distribution reached after three Gyr integration in MC17 potential (second row). There is a redistribution of particles both in the coordinate and in the velocity space. As one can see, the rearrangement of the azimuthal velocity of the particles V_ϕ is noticeable. After three Gyr, there is seen the appearance of thin diagonal ridges. These ridges, seen also in simulations by Antoja et al. [5] and Fux [60], Minchev et al. [61], Gómez et al. [62], result from the phase-space mixing in the plane of the disk that has initial distribution out of equilibrium [5]. The equilibrium distribution established in the axisymmetric potential after three Gyr of integration was taken as the initial distribution to simulate the dynamics of the disk dynamics in the models with a bar.

3.2. Dynamics in a Barred Potential

3.2.1. Resonances in the Plane of the Disk

Figure 6 demonstrates distribution of stars along the radius in four models with bar potential after three Gyr of evolution from the equilibrium state. The positions of corotation, OLR and 1:1 resonances are marked on the figure with the vertical lines. One can see the correlation of the dips on the distribution of particles along the radius with the position of the outer Lindblad resonance, especially noticeable in the models with the fast rotating bar. This result is known from previous studies (see, e.g., Melnik [63]). Stars near the OLR resonance change their angular momenta, which affects the orbits, eventually causing the radial migration of the stars. The process can move the stars radially by kiloparsecs [9,64].

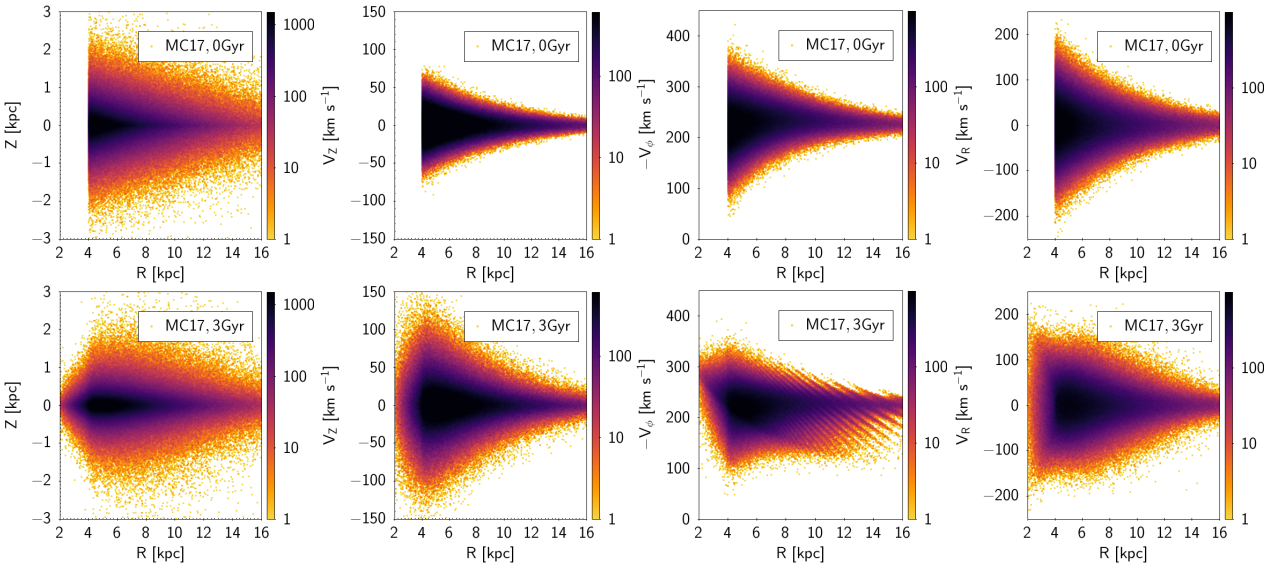

Figure 5. Rearrangement of the initially generated distribution in the MC17 potential (top frames) after three Gyr of evolution (bottom frames). First column—the distribution of stars along the radius, second, third, and fourth columns distributions of V_Z, V_ϕ and V_R velocity components along the radius. Particles' density distributions are encoded in the colour bars.

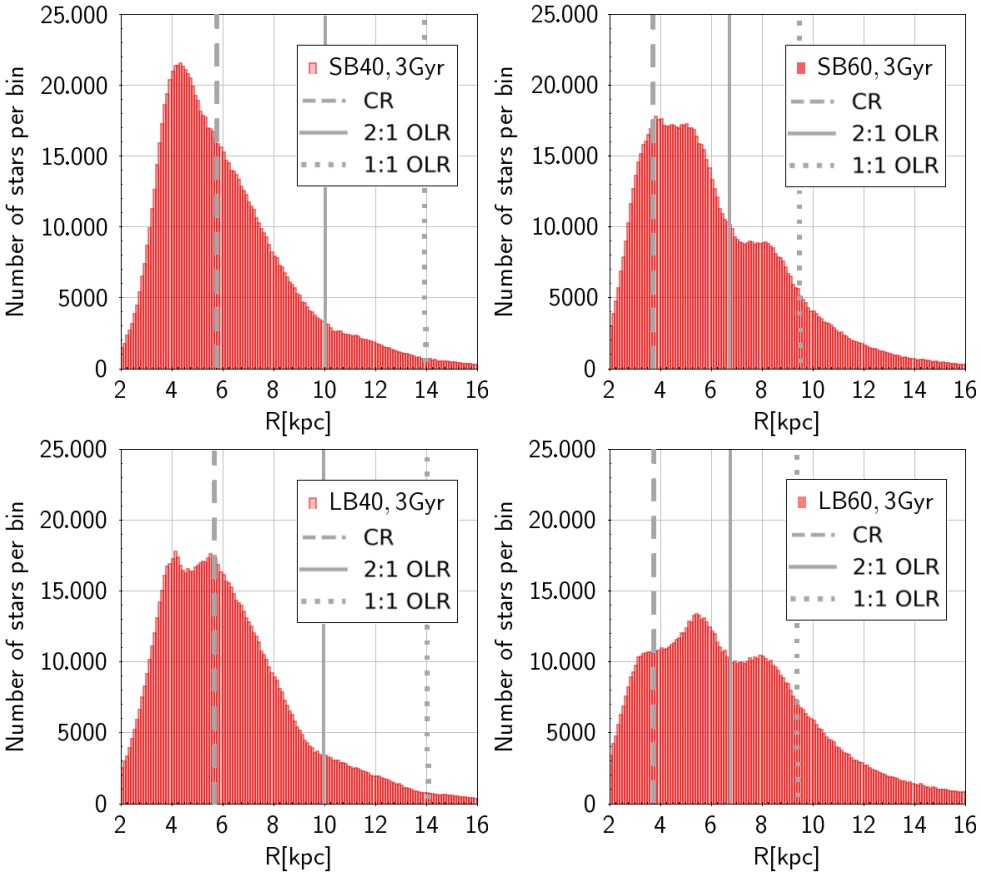

Figure 6. Radial distributions of particles in four barred potentials after three Gyr of evolution (SB40 top left; SB60 top right; LB40 bottom left; LB60 bottom right). The size of the radial bins is 0.1 kpc. The vertical dashed, solid and dotted lines show the positions of CR, 2:1 OLR and 1:1 OLR, respectively.

Figure 7 shows the distribution of stars in (R, Z), (R, V_Z) and (R, V_ϕ) planes after three Gyr of orbits evolution in the barred potential. Diagrams (R, Z), (R, V_Z) do not show a noticeable effect of the bar potential on the distribution of the particles at OLR resonances. The role of the 2:1 outer Lindblad resonance is revealed, however, as a decreasing of density of particles at OLR resonance in models with the fast rotating bar ($\Omega_b = 60\,\mathrm{km\ s^{-1}\ kpc^{-1}}$) due to proximity in these models of resonance to the bar region as shown in Figure 6. The influence of the OLR resonances on the distribution of particles is also illustrated in the (R, V_ϕ)-diagram of Figure 7, which shows the appearance of noticeable diagonal ridges seen on the figure. Similar ridges, confirmed observationally [6], are connected to the resonant orbital structure in the barred potential that forms regions in the phase space with stable and unstable orbits, and hence the regions with overdensities and gaps [5,65,66].

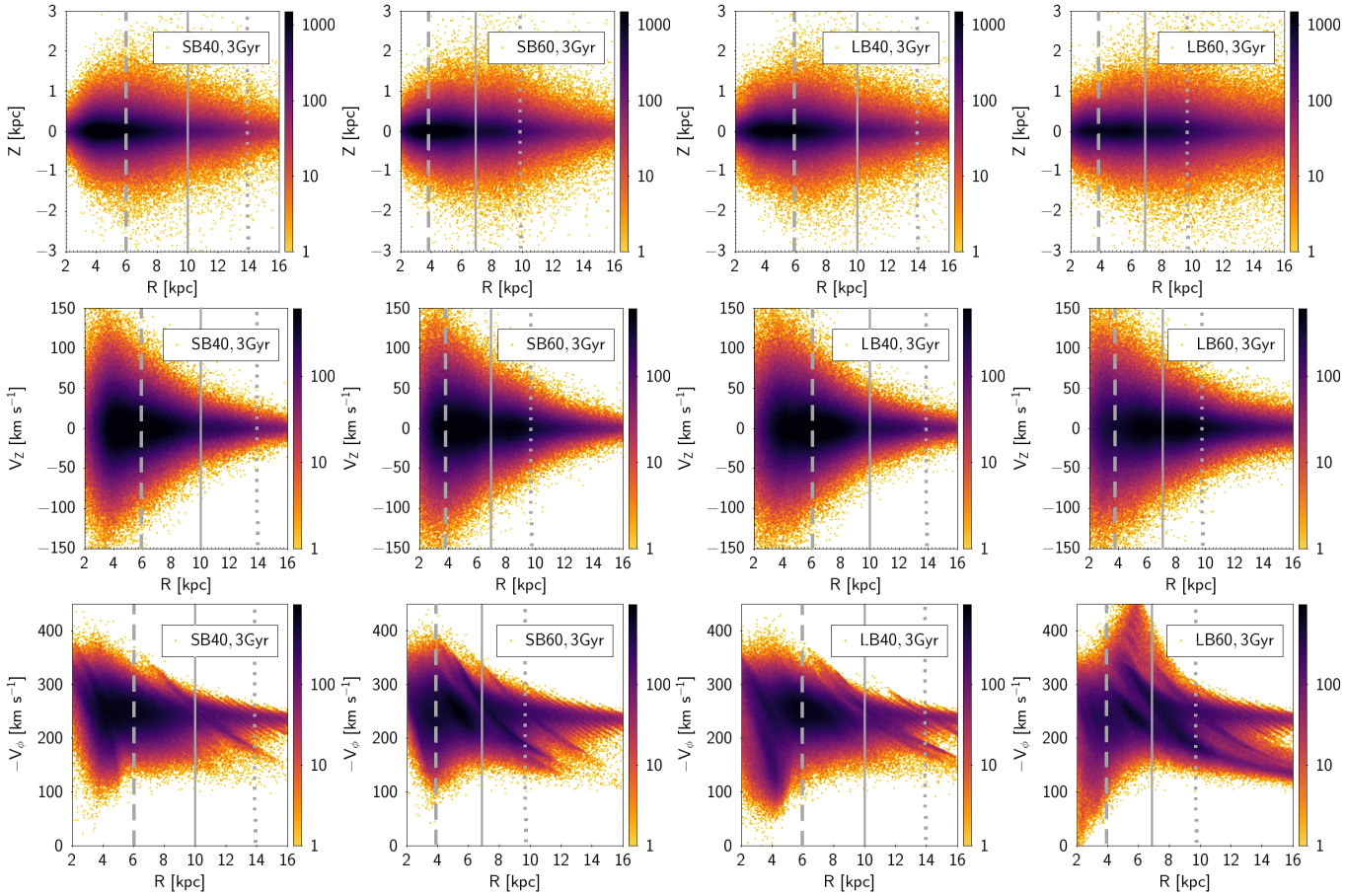

Figure 7. Distribution of particles shown on (R, Z)—plane (first row), (R, V_Z)—plane (second row), and (R, V_ϕ)—plane (third row) after three Gyr of evolution in models SB40 (first column), SB60 (second column), LB40 (third column), and LB60 (fourth column). The vertical dashed, solid and dotted lines show positions of CR, 2:1 OLR and 1:1 OLR, respectively.

To demonstrate the influence of resonances occurring in the plane of the disk on the disk's vertical structure, we follow Trick et al. [22] and describe the dynamics of the disk in $(L_Z, <|V_Z|>)$ and $(L_Z, <|Z|>)$ space. Figure 8 shows $(L_Z, <|Z|>)$ and $(L_Z, <|V_Z|>)$ distributions after three Gyr of evolution of the models for moving averages of the values $|Z|$ and $|L_Z|$. As is seen from Figure 8, the position of 2:1 OLR resonance correlates with the bumps on the $|Z|$ distribution of particles in all models. The dependence of the velocity component V_Z on radius is also affected by bar at the 2:1 OLR resonance region. The upper right panel of Figure 8 shows an elevation of $<|V_Z|>$ velocity in the vicinity of 2:1 outer Lindblad resonance in the model with the fast rotating long bar. A similar result was reported by Trick et al. [22] (see their Figure 9c), who also demonstrated that the 2:1

OLR resonance with the bar can contribute to the peculiarities in distribution of V_Z along the L_Z. To find the location of the resonances in L_Z space in Figure 8, we use the radial positions corresponding to the axisymmetric potential and the velocities corresponding to the rotation curve of MC17.

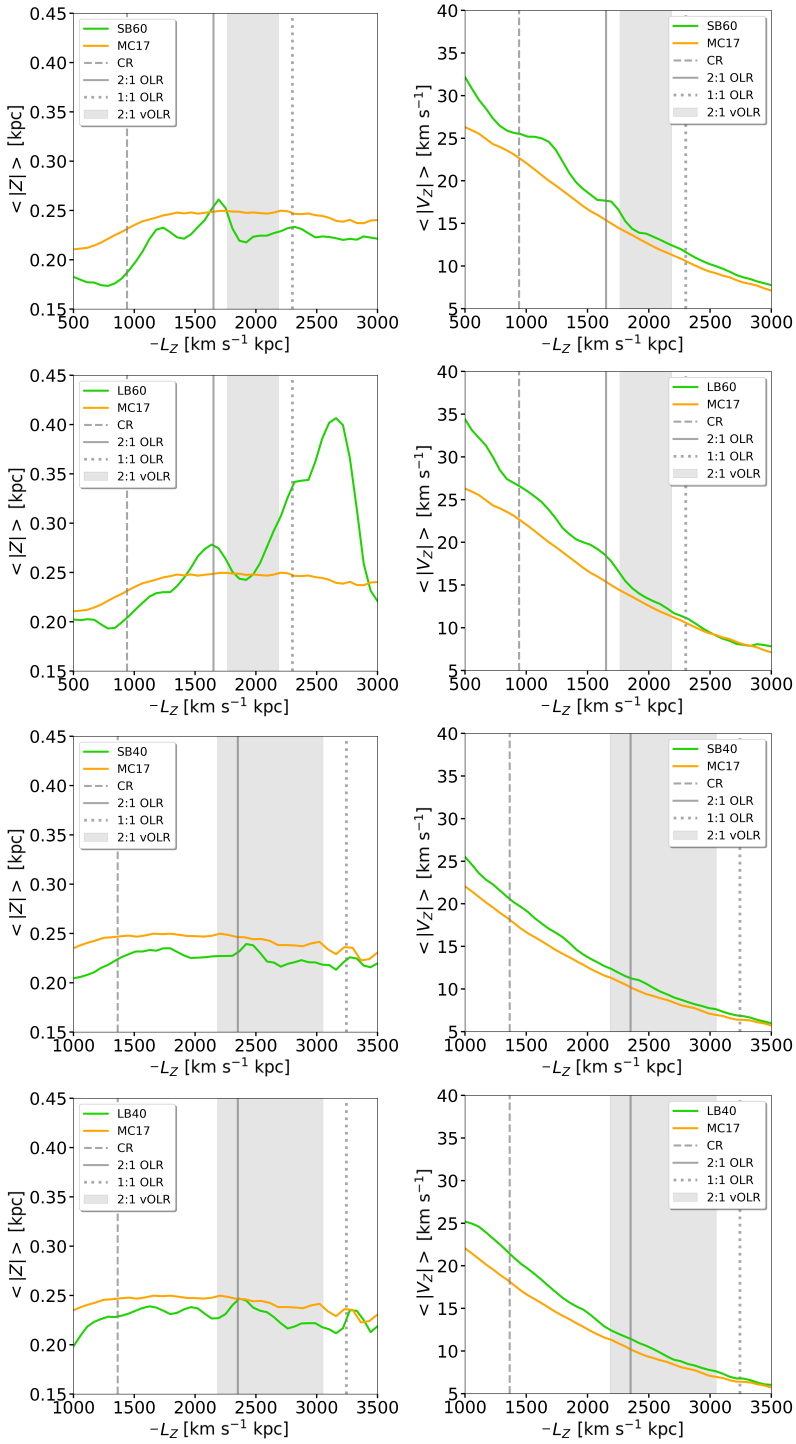

Figure 8. Green lines—average coordinate $< |Z| >$ (left column) and average velocity component $< |V_Z| >$ (right column) as functions of the angular momentum L_Z after three Gyr of evolution in barred potentials (SB60-first row, LB60-second row, SB40-third row and LB40 fourth row). Orange lines are the same as for green ones, but for the model MC17.

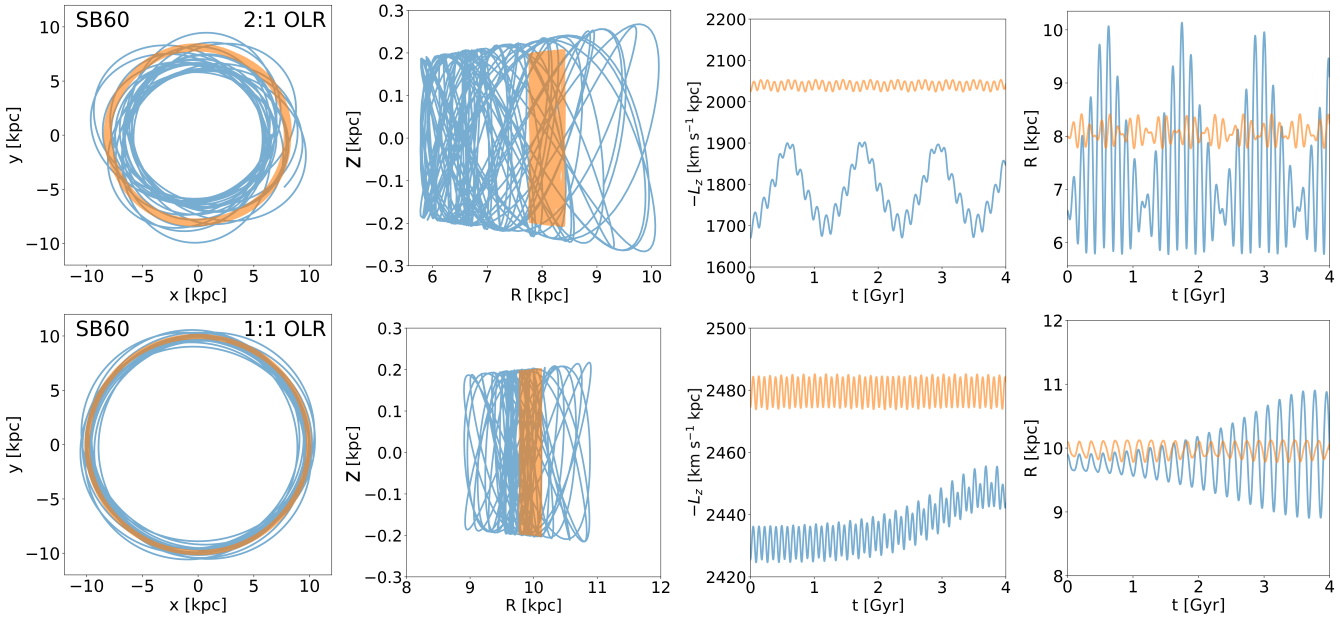

Figure 9. Evolution of resonant (blue) and non-resonant (orange) particles in model SB60 shown on (x, y), (R, Z), $(t, -L_Z)$ and (t, R)—planes at 2:1 (top row) and 1:1 (bottom row) OLR.

In models with a slowly rotating bar (SB40 and LB40), the influence of the 2:1 OLR on disk dynamics in the perpendicular direction is less noticeable due to its further location from the galactic center. The Z-distribution of the particles along the radius is perturbed by a few percent around the 2:1 outer Lindblad resonance. The influence of the 2:1 OLR on the particles V_Z distribution alone is negligible.

To clarify in more detail the influence of resonances on $(-L_Z, < |Z| >)$ and $(-L_Z, < |V_Z| >)$ distributions, we trace the dynamics of the resonant and non-resonant particles in the model with the short fast rotating bar SB60. Figure 9 shows the evolution of resonant (blue) and non-resonant (orange) particles at 2:1 (top row) and 1:1 (bottom row) outer Lindblad resonances. As one can see from the $L_Z - t$ plot in Figure 9, the angular momentum of resonant particles shows an oscillational behavior atop of the smaller time-scale oscillations, corresponding to the periodic disturbances from the bar, i.e., there is an oscillational behavior with a larger period. Similar behavior of the particles at the 2:1 outer Lindblad resonance was reported by Melnik [63], who gave an explanation for such behavior. Such behavior of the resonant particles influences the properties of the disk in the Z-direction. As one can see from Figure 9, the resonant particles can deviate up to 10 kpc from the resonance region, located at ≈ 6.5 kpc, bringing the particles with higher velocity dispersion σ_z to the regions with smaller values of z-component of the velocity dispersion of the disk, which leads to the appearance of a bump on $< Z >$–L_Z distribution in Figure 8.

Let us discuss in more detail the $(-L_Z, < |Z| >)$-distribution of the particles in LB60 model. Figure 8 shows that particles with angular momenta of $\approx$ 2200–2800 km s^{-1} kpc considerably increase the thickness of the disk with an average growth of the Z-coordinate of one hundred percent. The appearance of a bump on $(-L_Z, < |Z| >)$-diagram is related to the 'escapers'—the particles at the 2:1 OLR region that have amplitudes of oscillations large enough so the particles reach the bar region, and get an additional "kick" from a bar. Figure 10 supports this picture. As one can see from (t, L_Z) diagram of this figure, most of the resonant particles have a 'typical' behavior at the resonant region with angular momenta nonlinearly oscillating around the equilibrium value. A few percent of the particles that closely approach the bar region increase their angular momenta from from $-L_Z \approx$ 1600–1800 to 2200–3000 km s^{-1} kpc, reaching as a consequence large distances, both in radius and in the direction perpendicular to the disk. Khoperskov et al. [67] reported about the formation of the escaping particles from the OLR-region due to an

interaction with a slowing bar. Our simulations show that the formation of escapers occurs in a constantly rotating bar potential as well.

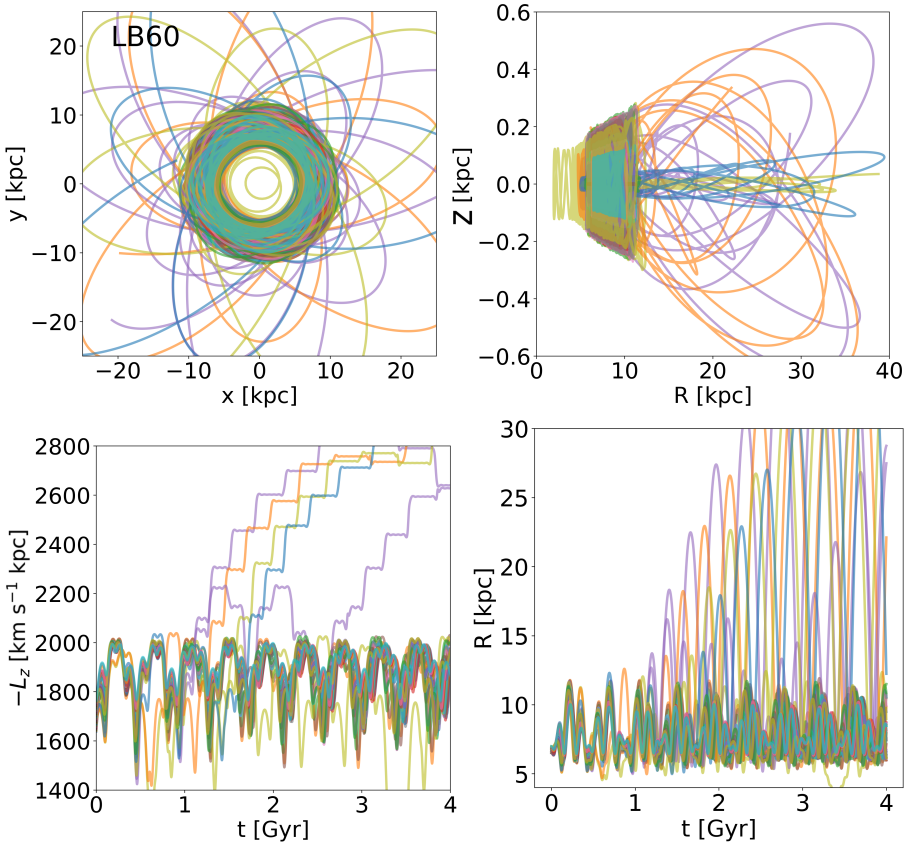

Figure 10. Orbit evolution of escaping particles in the model LB60 shown on (x, y), (R, Z), $(t, -L_Z)$ and (t, R)-planes.

The dynamics of resonant particles in the model LB60 with the fast elongated bar has some other features not seen in the models with a shorter (SB60) or a slowly rotating bar (SB40 and LB40). Figure 11 shows evolution of the particles in the LB60 model shown in (L_Z, Z), (R, V_ϕ) and (R, V_R)-planes over three Gyr of evolution. The (L_Z, Z)-plane of this figure demonstrates growth of the resonant structure for $L_Z \approx 2000$–3000 km s^{-1} kpc. We already discussed this feature also seen in Figure 8.

Another manifestation of escaping particles, shown in Figure 10, is the growth with time of high-velocity and low-velocity "tails", seen on the (R, V_ϕ) distributions of Figure 11. The origin of the tails is related to the escaping particles, which, due to the resonant set-up at the 2:1 outer Lindblad resonance, come close enough to the bar and deviate far from their original locations. The orbits of such resonant particles, occupying a relatively narrow band of angular momenta $L_Z \approx 2200$–2800 km s^{-1} kpc, become more elongated with time, with growing apocentric distances and pericentric velocities of the particles seen on the (R, V_ϕ) diagram of Figure 11 as high- and low-velocity tails.

The bottom row of Figure 11 shows the formation of chevron-like structures in the (R, V_R) distribution of the particles interacting with the long fast bar. Chevron-like structures are observed in the velocity distribution of the Milky Way halo stars [68,69], and were recently discovered in the Andromeda galaxy by Dey et al. [70]. Davies et al. [68], Belokurov et al. [69] and Wenbo Wu [71] suggest that such structures can result from accretion of a few satellite galaxies in the past of the Milky Way's history. Interaction of stars with a bar at corotation resonance can also lead to the formation of chevron-like structures, as shown recently by Dillamore et al. [72]. Our simulations demonstrate that chevrons can also be formed by the particles escaping from the 2:1 outer Lindblad resonance due to a strong

interaction with the fast long bar. We find that about five percent of the resonant stars are involved in the escaping process, and the formation of the chevron-like structures and tails. The formation of chevron-like structures by the escapees from the OLR region, requires, however, a more detailed study.

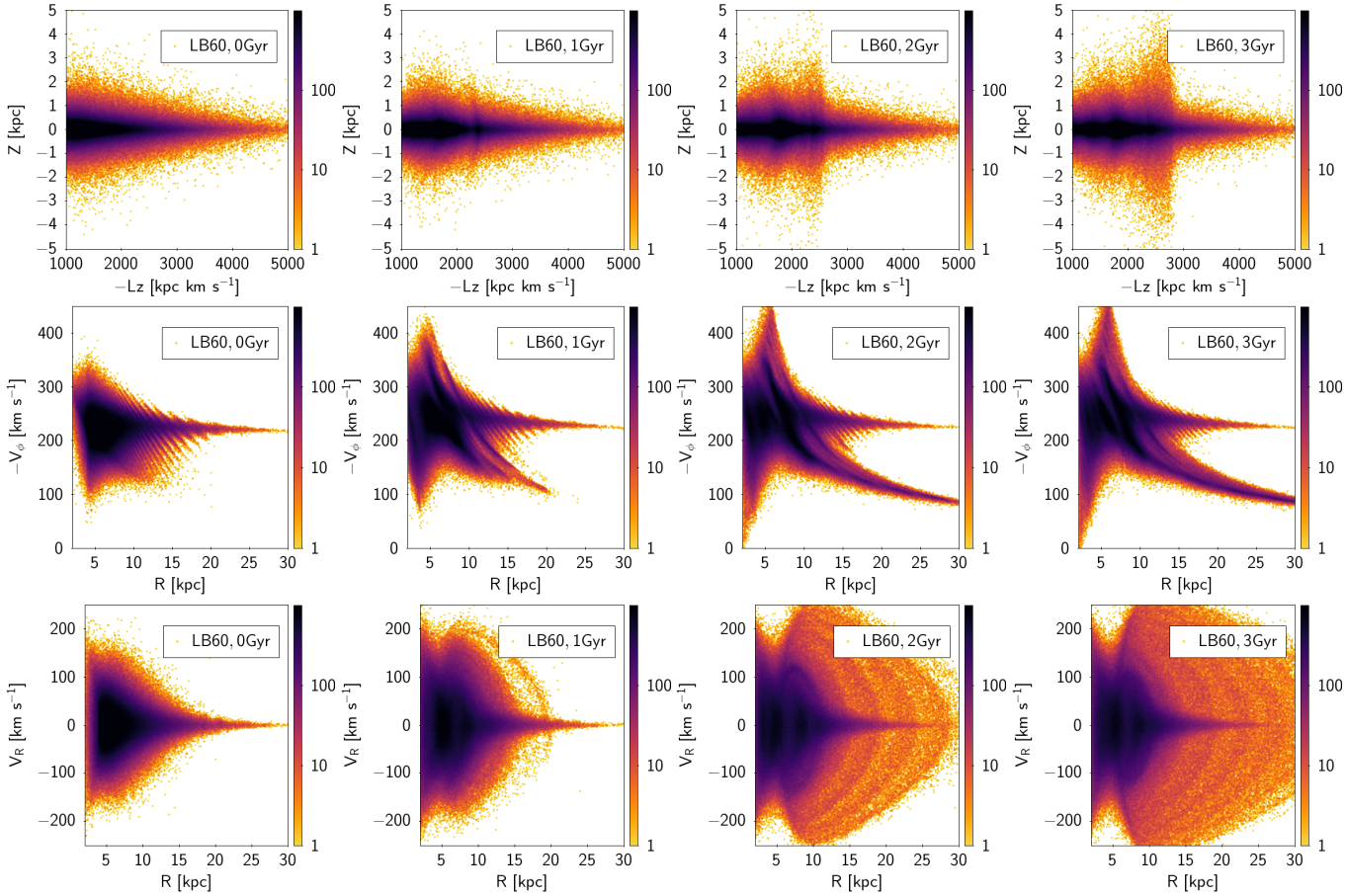

Figure 11. Evolution of (Z) (first row), (V_ϕ) (second row), and (V_R) (third row) distributions of particles in LB60 model.

It should be noted that such effects appear only in the LB60 model, for which a fast rotation provides a 2:1 OLR resonance position closer to the centre (near 7 kpc), unlike the slow bar (10 kpc). The parameters of the Milky Way bar, such as the length of the semi-major axis and the angular velocity of rotation, are still largely uncertain and it is not possible to draw an unambiguous conclusion about whether the LB60 model is acceptable for our galaxy. But it should also be noted that in the observational data of other galaxies there are both very rapidly rotating bars and long bars [73], in which such resonant effects may take place. However, the observation of structures such as chevrons, or high and low-velocity "tails" remain difficult or impossible tasks. However, such bar configurations (fast rotation and long major semi-axis) are quite rare for Milky Way Analogue galaxies [74].

3.2.2. Resonance with Motions Perpendicular to the Disk Direction

Let us discuss the influence of the 2:1 vertical outer Lindblad resonance occurring in the solar neighborhood on the disk's vertical structure if the angular velocity of the bar is equal to 60 km s^{-1} kpc. For resonant buildup of oscillations, it is necessary that the azimuthal variation of the vertical force from the perturbing potential of a bar be considerable. We find that the model LB60, with its fast rotating and elongated bar, satisfies this criterion. To demonstrate the influence of 2:1 vOLR, we follow the dynamics of two test particles in the resonance region, and integrate their orbits in the model LB60 with the fast rotating

elongated bar. These particles have initially circular orbits with initial $R = 8$ kpc, but differ by frequencies of oscillations in the direction perpendicular to the plane of the disk. The first particle has a frequency of oscillations equal to $\nu_Z \approx 9.7$ Gyr^{-1}, corresponding to the resonant frequency of oscillations at eight kpc (see Figure 2b). Another particle has a non-resonant frequency perpendicular to the disk direction equal to $\nu_Z \approx 12$ Gyr^{-1}. Figure 12 demonstrates the dynamics of the resonant and the non-resonant particles. As can be seen from the figure, in the plane of the disk, both particles have close to circular orbits, and oscillate along the radius with approximately the same amplitude. However, the particles demonstrate different behavior when perpendicular to the disk direction. Non-resonant particles (orange line) oscillate with constant amplitudes in both the coordinate Z and velocity V_Z. The resonant particles (blue line) oscillate perpendicular to the disk with periodically increasing and decreasing amplitudes of oscillations of Z and V_Z values.

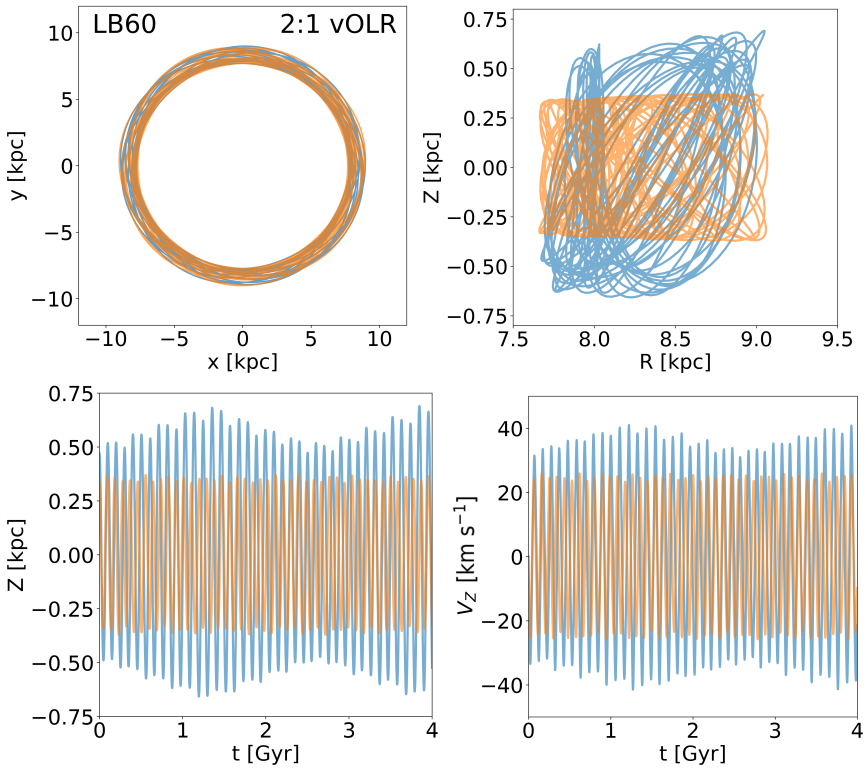

Figure 12. Dynamics of resonant (blue) and non-resonant (orange) particles shown in the model LB60 on (x, y), (R, Z), (t, Z) and (t, V_Z) planes at 2:1 vOLR.

It should be noticed that the resonance with the particle motions perpendicular to the plane of the disk occurs at eight kpc if the velocities of the particles in that direction are about $V_Z \approx 33$ km s^{-1} at Z = 0. Taking into account that the velocity dispersion of the thin disk in the solar neighborhood is equal to $\sigma_Z = 11$ km s^{-1}, there is a small number of such stars. Moreover, we find that 2:1 vOLR resonance occurs if stars are in nearly circular orbits. Also, the build up of resonance oscillations depends on the phase of a star's motion perpendicular to the disk relative to the phase of a rotating bar. Taking these factors into account, we conclude that it is unfeasible to observationally confirm a manifestation of the 2:1 vertical resonance in the solar neighborhood.

4. Summary

The results of our study can be summarized as follows.

In agreement with previous studies, we confirm that 2:1 OLR resonance of particles orbiting in the plane of the disk with the rotating bar leads to their spatial redistribution. The angular momenta of the resonant stars change under the influence of the bar. The

maximum of such momentum exchange occurs at 2:1 outer Lindblad resonance. The momentum exchange has oscillational behavior when atop of the smaller time-scale oscillations corresponding to the periodic disturbances from the rotating bar, i.e., there are oscillations with a larger period.

Spatial redistribution of the particles caused by their interaction with the potential of a bar is more prominent for a larger bar's semi-axis and its angular velocity is larger due to the fact that resonances in this case are closer to the perturbing potential. In addition to the redistribution of particles at OLR we find—in agreement with previous studies (Antoja et al. [5])—that resonance leads to the formation of the ridges seen in (R, V_ϕ) particles distribution.

The 2:1 and 1:1 OLR do not cause any noticeable influence on the distribution of particles and their velocities when perpendicular to the plane of the disk direction as a function of the radius. Such influence is seen, however, in the distributions of the average coordinate of the particles, $< |Z| >$ and their average velocity components, $< |V_Z| >$, as a function of the angular momentum L_Z. The effect manifests itself as bumps on L_Z—$< |Z| >$ and L_Z–$< |V_Z| >$-distributions developing outside the resonance region.

Simulations show an appearance of prominent bump of the average coordinate of the particles, $< |Z| >$ as a function of the momentum L_Z at $\approx$ 2200–2800 km s^{-1} kpc in the model with a long, fast bar. Appearance of the bump on $(-L_Z, < |Z| >)$—diagram is related to the 'escapers'—the particles at 2:1 OLR region that have the amplitudes of oscillations grown large enough so they reach the bar region. Strong interaction with the bar potential of such resonant particles provides an additional "kick" from a bar. We find that a few percent of the particles in the vicinity of the 2:1 OLR can closely approach the bar region and increase their angular momenta from $-L_Z \approx$ 1600–1800 to 2200–3000 km s^{-1} kpc, propagating, as a consequence, at large distances both in radius and in the direction perpendicular to the disk.

The escaping stars in the model with a long fast bar generate and strengthen with time the high- and low-velocity "tails" seen on the (R, V_ϕ)—particle distribution.

Another manifestation of the 2:1 resonance in the LB60 model is the appearance of the chevron-like structures seen on the R, V_R diagram. Such structures are observed in the Milky Way halo and assumed to be the result of an accretion of a massive satellite galaxy into the Milky Way. Our simulations demonstrate that chevrons can also be formed by the particles escaping from the 2:1 outer Lindblad resonance due to a strong interaction with the fast long bar.

The resonance of the particle motions in the direction perpendicular to the plane of the disk with the rotating bar (vOLR–resonance) can also affect the disk's kinematical properties in the direction perpendicular to its plane. We find that the "vertical resonance" can amplify the amplitude of oscillations of resonance particles by about a hundred percent. The condition for the vertical resonance in the solar neighborhood is not, however, satisfied for all particles. Only particles, that have at the solar neighborhood the velocity of $V_Z \approx$ 33 km s^{-1} at Z = 0 satisfy the resonance condition. Moreover, we find that 2:1 vOLR resonance occurs if stars have nearly circular orbits. In addition, the build-up of resonance oscillations depends on the phase of a star's motion perpendicular to the disk relative to the phase of a rotating bar. Taking these factors into account, we conclude that it is unfeasible to observationally confirm a manifestation of the 2:1 vertical resonance in the solar neighborhood.

The resonances 2:1 OLR and vOLR do not have any noticeable effect on V_Z-distribution of stars in the solar neghborhood. We conclude therefore that peculiarities of V_Z-velocity distribution in the solar neighborhood reported by Vieira et al. [32] cannot be caused by the influence of resonances with a rotating bar.

Author Contributions: Conceptualization, V.K., G.C., K.V. and R.T.; methodology, V.K., G.C. and R.T.; software, R.T. and A.L.; writing original draft preparation, V.K., R.T. and G.C.; writing review and editing, V.K., R.T., A.L., G.C. and K.V. All authors have read and agreed to the published version of the manuscript.

Funding: The research by V.K. and R.T. was carried out at Southern Federal University with the financial support of the Ministry of Science and Higher Education of the Russian Federation (State contract GZ0110/23-10-IF).

Data Availability Statement: All data used in this paper are taken from the open sources and the references are given.

Acknowledgments: We thank the anonymous reviewers for the careful reading of the manuscript and valuable comments.

Conflicts of Interest: The authors declare no conflict of interest.

Abbreviations

The following abbreviations are used in this manuscript:

Corotation Resonance	CR
inner Lindblad resonance	ILR
outer Lindblad resonance	OLR
vertical outer Lindblad resonance	vOLR
Long bar	LB
Short bar	SB
MC17	McMillan17

References

1. Perryman, M.A.C.; de Boer, K.S.; Gilmore, G.; Høg, E.; Lattanzi, M.G.; Lindegren, L.; Luri, X.; Mignard, F.; Pace, O.; de Zeeuw, P.T. GAIA: Composition, formation and evolution of the Galaxy. *Astron. Astrophys.* **2001**, *369*, 339–363. [CrossRef]
2. Lindegren, L.; Lammers, U.; Bastian, U.; Hernández, J.; Klioner, S.; Hobbs, D.; Bombrun, A.; Michalik, D.; Ramos-Lerate, M.; Butkevich, A.; et al. Gaia Data Release 1. Astrometry: One billion positions, two million proper motions and parallaxes. *Astron. Astrophys.* **2016**, *595*, A4.
3. Fabricius, C.; Bastian, U.; Portell, J.; Castañeda, J.; Davidson, M.; Hambly, N.C.; Clotet, M.; Biermann, M.; Mora, A.; Busonero, D.; et al. Gaia Data Release 1. Pre-processing and source list creation. *Astron. Astrophys.* **2016**, *595*, A3.
4. Evans, D.W.; Riello, M.; De Angeli, F.; Carrasco, J.M.; Montegriffo, P.; Fabricius, C.; Jordi, C.; Palaversa, L.; Diener, C.; Busso, G.; et al. Gaia Data Release 2. Photometric content and validation. *Astron. Astrophys.* **2018**, *616*, A4.
5. Antoja, T.; Helmi, A.; Romero-Gómez, M.; Katz, D.; Babusiaux, C.; Drimmel, R.; Evans, D.W.; Figueras, F.; Poggio, E.; Reylé, C.; et al. A dynamically young and perturbed Milky Way disk. *Nature* **2018**, *561*, 360–362.
6. Kawata, D.; Baba, J.; Ciucă, I.; Cropper, M.; Grand, R.J.J.; Hunt, J.A.S.; Seabroke, G. Radial distribution of stellar motions in Gaia DR2. *Mon. Not. R. Astron. Soc.* **2018**, *479*, L108–L112.
7. Khanna, S.; Sharma, S.; Tepper-Garcia, T.; Bland-Hawthorn, J.; Hayden, M.; Asplund, M.; Buder, S.; Chen, B.; De Silva, G.M.; Freeman, K.C.; et al. The GALAH survey and Gaia DR2: Linking ridges, arches, and vertical waves in the kinematics of the Milky Way. *Mon. Not. R. Astron. Soc.* **2019**, *489*, 4962–4979.
8. Schönrich, R.; Binney, J. Origin and structure of the Galactic disc(s). *Mon. Not. R. Astron. Soc.* **2009**, *399*, 1145–1156.
9. Sellwood, J.A.; Binney, J.J. Radial mixing in galactic discs. *Mon. Not. R. Astron. Soc.* **2002**, *336*, 785–796.
10. Roškar, R.; Debattista, V.P.; Quinn, T.R.; Stinson, G.S.; Wadsley, J. Riding the Spiral Waves: Implications of Stellar Migration for the Properties of Galactic Disks. *Astrophys. J.* **2008**, *684*, L79.
11. Laughlin, G.; Korchagin, V. Nonlinear Generation of One-armed Spirals in Self-gravitating Disks. *Astrophys. J.* **1996**, *460*, 855. [CrossRef]
12. Dehnen, W. The Effect of the Outer Lindblad Resonance of the Galactic Bar on the Local Stellar Velocity Distribution. *Astron. J.* **2000**, *119*, 800–812.
13. Antoja, T.; Helmi, A.; Dehnen, W.; Bienaymé, O.; Bland-Hawthorn, J.; Famaey, B.; Freeman, K.; Gibson, B.K.; Gilmore, G.; Grebel, E.K.; et al. Constraints on the Galactic bar from the Hercules stream as traced with RAVE across the Galaxy. *Astron. Astrophys.* **2014**, *563*, A60.
14. Monari, G.; Kawata, D.; Hunt, J.A.S.; Famaey, B. Tracing the Hercules stream with Gaia and LAMOST: New evidence for a fast bar in the Milky Way. *Mon. Not. R. Astron. Soc.* **2017**, *466*, L113–L117.
15. Hunt, J.A.S.; Bovy, J. The 4:1 outer Lindblad resonance of a long-slow bar as an explanation for the Hercules stream. *Mon. Not. R. Astron. Soc.* **2018**, *477*, 3945–3953.
16. Hunt, J.A.S.; Hong, J.; Bovy, J.; Kawata, D.; Grand, R.J.J. Transient spiral structure and the disc velocity substructure in Gaia DR2. *Mon. Not. R. Astron. Soc.* **2018**, *481*, 3794–3803.
17. Binney, J.; Schönrich, R. The origin of the Gaia phase-plane spiral. *Mon. Not. R. Astron. Soc.* **2018**, *481*, 1501–1506.
18. Tepper-García, T.; Bland-Hawthorn, J.; Freeman, K. Galactic seismology: Joint evolution of impact-triggered stellar and gaseous disc corrugations. *Mon. Not. R. Astron. Soc.* **2022**, *515*, 5951–5968.

19. Chequers, M.H.; Widrow, L.M.; Darling, K. Bending waves in the Milky Way's disc from halo substructure. *Mon. Not. R. Astron. Soc.* **2018**, *480*, 4244–4258.
20. Khoperskov, S.; Di Matteo, P.; Gerhard, O.; Katz, D.; Haywood, M.; Combes, F.; Berczik, P.; Gomez, A. The echo of the bar buckling: Phase-space spirals in Gaia Data Release 2. *Astron. Astrophys.* **2019**, *622*, L6. [CrossRef]
21. Khachaturyants, T.; Beraldo e Silva, L.; Debattista, V.P.; Daniel, K.J. Bending waves excited by irregular gas inflow along warps. *Mon. Not. R. Astron. Soc.* **2022**, *512*, 3500–3519.
22. Trick, W.H.; Fragkoudi, F.; Hunt, J.A.S.; Mackereth, J.T.; White, S.D.M. Identifying resonances of the Galactic bar in Gaia DR2: I. Clues from action space. *Mon. Not. R. Astron. Soc.* **2021**, *500*, 2645–2665.
23. Mishurov, Y.N.; Tkachenko, R.V. On the radial oxygen distribution in the Galactic disc. *Mon. Not. R. Astron. Soc.* **2018**, *473*, 3700–3709. [CrossRef]
24. Mishurov, Y.N.; Tkachenko, R.V. On the radial iron distribution in the Galactic disc. *Mon. Not. R. Astron. Soc.* **2019**, *485*, 2225–2234. [CrossRef]
25. Mishurov, Y.N.; Tkachenko, R.V. Local Metallicity Distribution Function Derived from Galactic Large-scale Radial Iron Pattern Modeling. *Astrophys. J.* **2019**, *887*, 238.
26. Khoperskov, S.; Gerhard, O. Chemo-kinematics of the Milky Way spiral arms and bar resonances: Connection to ridges and moving groups in the solar vicinity. *Astron. Astrophys.* **2022**, *663*, A38.
27. Binney, J. Resonant excitation of motion perpendicular to galactic planes. *Mon. Not. R. Astron. Soc.* **1981**, *196*, 455–467. [CrossRef]
28. Combes, F.; Debbasch, F.; Friedli, D.; Pfenniger, D. Box and peanut shapes generated by stellar bars. *Astron. Astrophys.* **1990**, *233*, 82.
29. Quillen, A.C. Growth of a Peanut-shaped Bulge via Resonant Trapping of Stellar Orbits in the Vertical Inner Lindblad Resonances. *Astron. J.* **2002**, *124*, 722–732.
30. Quillen, A.C.; Minchev, I.; Sharma, S.; Qin, Y.J.; Di Matteo, P. A vertical resonance heating model for X- or peanut-shaped galactic bulges. *Mon. Not. R. Astron. Soc.* **2014**, *437*, 1284–1307.
31. Fouvry, J.B.; Pichon, C.; Chavanis, P.H.; Monk, L. Resonant thickening of self-gravitating discs: Imposed or self-induced orbital diffusion in the tightly wound limit. *Mon. Not. R. Astron. Soc.* **2017**, *471*, 2642–2673.
32. Vieira, K.; Carraro, G.; Korchagin, V.; Lutsenko, A.; Girard, T.M.; van Altena, W. Milky Way Thin and Thick Disk Kinematics with Gaia EDR3 and RAVE DR5. *Astrophys. J.* **2022**, *932*, 28.
33. Bovy, J. galpy: A python Library for Galactic Dynamics. *Astrophys. J. Suppl. Ser.* **2015**, *216*, 29.
34. Alexander, R. Solving Ordinary Differential Equations I: Nonstiff Problems (E. Hairer, SP Norsett, and G. Wanner). *SIAM Rev.* **1990**, *32*, 485–486. [CrossRef]
35. Drimmel, R.; Spergel, D.N. Three-dimensional Structure of the Milky Way Disk: The Distribution of Stars and Dust beyond 0.35 R_{solar}. *Astrophys. J.* **2001**, *556*, 181–202.
36. Gerhard, O.E. Structure and Mass Distribution of the Milky Way Bulge and Disk. In Proceedings of the Galaxy Disks and Disk Galaxies, Rome, Italy, 12–16 January 2001; Astronomical Society of the Pacific Conference Series, San Francisco, U.S.; Funes, J.G., Corsini, E.M., Eds.; 2001; Volume 230, pp. 21–30.
37. Piffl, T.; Binney, J.; McMillan, P.J.; Steinmetz, M.; Helmi, A.; Wyse, R.F.G.; Bienaymé, O.; Bland-Hawthorn, J.; Freeman, K.; Gibson, B.; et al. Constraining the Galaxy's dark halo with RAVE stars. *Mon. Not. R. Astron. Soc.* **2014**, *445*, 3133–3151.
38. Khrapov, S.; Khoperskov, A.; Korchagin, V. Modeling of Spiral Structure in a Multi-Component Milky Way-Like Galaxy. *Galaxies* **2021**, *9*, 29.
39. Jurić, M.; Ivezić, Ž.; Brooks, A.; Lupton, R.H.; Schlegel, D.; Finkbeiner, D.; Padmanabhan, N.; Bond, N.; Sesar, B.; Rockosi, C.M.; et al. The Milky Way Tomography with SDSS. I. Stellar Number Density Distribution. *Astrophys. J.* **2008**, *673*, 864–914.
40. Kordopatis, G.; Recio-Blanco, A.; de Laverny, P.; Gilmore, G.; Hill, V.; Wyse, R.F.G.; Helmi, A.; Bijaoui, A.; Zoccali, M.; Bienaymé, O. A spectroscopic survey of thick disc stars outside the solar neighbourhood. *Astron. Astrophys.* **2011**, *535*, A107.
41. McMillan, P.J. The mass distribution and gravitational potential of the Milky Way. *Mon. Not. R. Astron. Soc.* **2017**, *465*, 76–94.
42. Tiede, G.P.; Terndrup, D.M. Kinematics, Metallicities, and Stellar Distributions in the Inner Disk and Bulge of the Milky Way. *Astron. J.* **1999**, *118*, 895–910. [CrossRef]
43. Long, K.; Murali, C. Analytical Potentials for Barred Galaxies. *Astrophys. J.* **1992**, *397*, 44. [CrossRef]
44. Portail, M.; Gerhard, O.; Wegg, C.; Ness, M. Dynamical modelling of the galactic bulge and bar: The Milky Way's pattern speed, stellar and dark matter mass distribution. *Mon. Not. R. Astron. Soc.* **2017**, *465*, 1621–1644.
45. Kent, S.M. Galactic Structure from the Spacelab Infrared Telescope. III. A Dynamical Model for the Milky Way Bulge. *Astrophys. J.* **1992**, *387*, 181. [CrossRef]
46. Zhao, H.; Spergel, D.N.; Rich, R.M. Signature of Bulge Triaxiality From Kinematics in Baade's Window. *Astron. J.* **1994**, *108*, 2154.
47. Debattista, V.P.; Gerhard, O.; Sevenster, M.N. The pattern speed of the OH/IR stars in the Milky Way. *Mon. Not. R. Astron. Soc.* **2002**, *334*, 355–368.
48. Sanders, J.L.; Smith, L.; Evans, N.W.; Lucas, P. Transverse kinematics of the Galactic bar-bulge from VVV and Gaia. *Mon. Not. R. Astron. Soc.* **2019**, *487*, 5188–5208.
49. Clarke, J.P.; Wegg, C.; Gerhard, O.; Smith, L.C.; Lucas, P.W.; Wylie, S.M. The Milky Way bar/bulge in proper motions: A 3D view from VIRAC and Gaia. *Mon. Not. R. Astron. Soc.* **2019**, *489*, 3519–3538.
50. Shen, J.; Zheng, X.W. The bar and spiral arms in the Milky Way: Structure and kinematics. *Res. Astron. Astrophys.* **2020**, *20*, 159.

51. Sormani, M.C.; Binney, J.; Magorrian, J. Gas flow in barred potentials—III. Effects of varying the quadrupole. *Mon. Not. R. Astron. Soc.* **2015**, *454*, 1818–1839.
52. Gardner, E.; Flynn, C. Probing the Galaxy's bars via the Hercules stream. *Mon. Not. R. Astron. Soc.* **2010**, *405*, 545–552.
53. Chakrabarty, D. Phase space structure in the solar neighbourhood. *Astron. Astrophys.* **2007**, *467*, 145–162. [CrossRef]
54. Bissantz, N.; Englmaier, P.; Gerhard, O. Gas dynamics in the Milky Way: Second pattern speed and large-scale morphology. *Mon. Not. R. Astron. Soc.* **2003**, *340*, 949–968.
55. Contopoulos, G. How far do bars extend. *Astron. Astrophys.* **1980**, *81*, 198–209.
56. Abuter, R.; Amorim, A.; Anugu, N.; Bauböck, M.; Benisty, M.; Berger, J.P.; Blind, N.; Bonnet, H.; Brandner, W.; Buron, A.; et al. Detection of the gravitational redshift in the orbit of the star S2 near the Galactic centre massive black hole. *Astron. Astrophys.* **2018**, *615*, L15.
57. Sellwood, J.A. Dynamics of Disks and Warps. In *Planets, Stars and Stellar Systems: Galactic Structure and Stellar Populations*; Oswalt, T.D., Gilmore, G., Eds.; Springer: Dordrecht, The Netherlands; 2013; Volume 5, p. 923. [CrossRef]
58. Sellwood, J.A.; Wilkinson, A. Dynamics of barred galaxies. *Rep. Prog. Phys.* **1993**, *56*, 173–256.
59. Beraldo e Silva, L.; Debattista, V.P.; Anderson, S.R.; Valluri, M.; Erwin, P.; Daniel, K.J.; Deg, N. Orbital support and evolution of flat profiles of bars (shoulders). *arXiv* **2023**, arXiv:2303.04828.
60. Fux, R. Order and chaos in the local disc stellar kinematics induced by the Galactic bar. *Astron. Astrophys.* **2001**, *373*, 511–535. [CrossRef]
61. Minchev, I.; Quillen, A.C.; Williams, M.; Freeman, K.C.; Nordhaus, J.; Siebert, A.; Bienaymé, O. Is the Milky Way ringing? The hunt for high-velocity streams. *Mon. Not. R. Astron. Soc.* **2009**, *396*, L56–L60.
62. Gómez, F.A.; Minchev, I.; Villalobos, Á.; O'Shea, B.W.; Williams, M.E.K. Signatures of minor mergers in Milky Way like disc kinematics: ringing revisited. *Mon. Not. R. Astron. Soc.* **2012**, *419*, 2163–2172.
63. Melnik, A.M. Galactic resonance rings: Modelling of motions in the wide solar neighbourhood. *Mon. Not. R. Astron. Soc.* **2019**, *485*, 2106–2124.
64. Mikkola, D.; McMillan, P.J.; Hobbs, D. Radial migration and vertical action in N-body simulations. *Mon. Not. R. Astron. Soc.* **2020**, *495*, 3295–3306.
65. Michtchenko, T.A.; Lépine, J.R.D.; Barros, D.A.; Vieira, R.S.S. Combined dynamical effects of the bar and spiral arms in a Galaxy model. Application to the solar neighbourhood. *Astron. Astrophys.* **2018**, *615*, A10.
66. Hunt, J.A.S.; Bub, M.W.; Bovy, J.; Mackereth, J.T.; Trick, W.H.; Kawata, D. Signatures of resonance and phase mixing in the Galactic disc. *Mon. Not. R. Astron. Soc.* **2019**, *490*, 1026–1043.
67. Khoperskov, S.; Di Matteo, P.; Haywood, M.; Gómez, A.; Snaith, O.N. Escapees from the bar resonances. Presence of low-eccentricity metal-rich stars at the solar vicinity. *Astron. Astrophys.* **2020**, *638*, A144.
68. Davies, E.Y.; Dillamore, A.M.; Vasiliev, E.; Belokurov, V. Accelerated phase-mixing in the stellar halo due to a rotating bar. *Mon. Not. R. Astron. Soc.* **2023**, *521*, L24–L28.
69. Belokurov, V.; Vasiliev, E.; Deason, A.J.; Koposov, S.E.; Fattahi, A.; Dillamore, A.M.; Davies, E.Y.; Grand, R.J.J. Energy wrinkles and phase-space folds of the last major merger. *Mon. Not. R. Astron. Soc.* **2023**, *518*, 6200–6215.
70. Dey, A.; Najita, J.R.; Koposov, S.E.; Josephy-Zack, J.; Maxemin, G.; Bell, E.F.; Poppett, C.; Patel, E.; Beraldo e Silva, L.; Raichoor, A.; et al. DESI Observations of the Andromeda Galaxy: Revealing the Immigration History of Our Nearest Neighbor. *Astrophys. J.* **2023**, *944*, 1.
71. Wu, W.; Zhao, G.; Chang, J.; Xue, X.-X.; Chen, Y.; Li, C.; Ye, X.; Yang, C. Detection of multiple phase space overdensities of GSE stars by orbit integration. *arXiv* **2023**, arXiv:2305.06759.
72. Dillamore, A.M.; Belokurov, V.; Evans, N.W.; Davies, E.Y. Stellar halo substructure generated by bar resonances. *arXiv* **2023**, arXiv:2303.00008.
73. Lee, Y.H.; Park, M.G.; Hwang, H.S.; Ann, H.B.; Chung, H.; Kim, T. Properties of Fast and Slow Bars Classified by Epicyclic Frequency Curves from Photometry of Barred Galaxies. *Astrophys. J.* **2022**, *926*, 58.
74. Garma-Oehmichen, L.; Hernández-Toledo, H.; Aquino-Ortíz, E.; Martinez-Medina, L.; Puerari, I.; Cano-Díaz, M.; Valenzuela, O.; Vázquez-Mata, J.A.; Géron, T.; Martínez-Vázquez, L.A.; et al. SDSS IV MaNGA: Bar pattern speed in Milky Way analogue galaxies. *Mon. Not. R. Astron. Soc.* **2022**, *517*, 5660–5677.